A fast method for quantifying observational selection effects in asteroid surveys

Robert Jedicke [a,*], Bryce Bolin [b], Mikael Granvik [c,d], Ed Beshore [e]

[a] Institute for Astronomy, University of Hawaii, 2680 Woodlawn Dr, Honolulu, HI 96822, United States
[b] Laboratoire Lagrange, Université Côte d'Azur, Observatoire de la Côte d'Azur, CNRS, Blvd de l'Observatoire, CS 34229, 06304 Nice cedex 4, France
[c] Department of Physics, P.O. Box 64, 00014 University of Helsinki, Finland
[d] Finnish Geospatial Research Institute, P.O. Box 15, 02430 Masala, Finland
[e] Lunar and Planetary Laboratory, University of Arizona, Tucson, AZ 85721, United States

ARTICLE INFO

ABSTRACT

We present a fast method to calculate an asteroid survey's 'bias' – essentially a correction factor from the observed number of objects to the actual number in the population. The method builds upon the work of Jedicke and Metcalfe (Jedicke, R., Metcalfe, T.S. [1998]. Icaurs 131, 245–260) and Granvik et al. (Granvik, M., Vaubaillon, J., Jedicke, R. [2012]. Icarus 218, 262–277) and essentially efficiently maps out the phase space of orbit elements that can appear in a field-of-view. It does so by 'integrating' outwards in geocentric distance along a field's boresite from the topocentric location of the survey and calculating the allowable angular elements for each desired combination of semi-major axis, eccentricity and inclination. We then use a contour algorithm to map out the orbit elements that place an object at the edge of the field-of-view. We illustrate the method's application to calculate the bias correction for near Earth Objects detected with the Catalina Sky Survey (Christensen, E. et al. [2012]. AAS/Division for Planetary Sciences Meeting Abstracts, vol. 44, p. 210.13; Larson, S. et al. [1998]. Bulletin of the American Astronomical Society, vol. 30, p. 1037).

© 2015 Elsevier Inc. All rights reserved.

1. Introduction

The critical key to measuring the true size and orbit distribution of an asteroid or comet population is the efficiency for detecting them *as a function of their size and orbit elements*, and the fidelity of the detection efficiency needs to improve in step with the number of known objects in the population in order that the corrected, unbiased, population estimate is not dominated by systematic errors and uncertainties. In this work we describe a faster method for calculating asteroid detection efficiency (also known as the 'bias correction') for modern high-statistics long-duration asteroid surveys that builds upon the methods described by Jedicke and Metcalfe (1998) and Jedicke et al. (2002).

There is a long history of attempting to determine the true number of asteroids in the solar system. For instance, Baade (1934) estimated that there are 30–40 thousand asteroids brighter than $V = 19$ on the sky using just 37 asteroids detected on 21 photographic plates. The methods he employed to correct for the loss in detection sensitivity as a function of the asteroid's trail length on the exposure were similar to those employed today with CCDs. His bias correction from the area covered by the 21 photographic plates to the entire sky relied on the 1200 asteroids known at the time but did not account for the difference in distance between main belt objects observed towards opposition and those in the direction of the Sun. Baade's (1934) estimate was $\gtrsim 10\times$ Jehkowsky's[1] estimate from just a year earlier but is in fairly good agreement with modern estimates – there are about 25,000 known asteroids with $V < 19$ more than $90°$ from the Sun, and the Solar System model of Grav et al. (2011) suggests that there are about 40,000 asteroids with $V < 19$ on the entire sky-plane.

The all-ecliptic McDonald Survey of Asteroids to $B \lesssim 16.5$ (Kuiper et al., 1958) and its extension, the 'deep' pencil-beam Palomar–Leiden Survey to $B \lesssim 20$ (PLS, van Houten et al., 1970), 'debiased' their results but it is difficult to compare the modern population to their values because of the different magnitude systems and their non-physical limitations on the population, e.g. restricting the population of objects to those with declination <18°. If we assume that the PLS absolute g magnitudes were photographic B and use a mean $B - V$ asteroid color of 0.75 (Tedesco,

---

[1] From Baade (1934): Jehkowsky, *Sur le nombre probable d'asterodes que l'on peut découvrir avec les moyens actuels d'observation.* C.R., 197, 579, 1933.

1995) then the PLS estimated that there are about 18,000 asteroids with absolute magnitude $H_V < 15.0$ in the declination strip. This is about half the number of *known* asteroids with $H_V < 15.0$ and inclinations $i < 9°$, corresponding roughly to those asteroids that are confined to ecliptic latitudes of $\beta \lesssim 18°$.

About 40 years ago Whipple (1973) stated that the frequency distribution of Apollo-type asteroids, those with perihelion distance < 1 au, 'remains quite uncertain'. He attempted to correct for the selection effects by using the fact that none of the 15 Apollo asteroids known at the time had been accidentally re-discovered. This allowed him to state with 50% confidence that the total number of Apollo asteroids with $H < 18$, roughly 1 km diameter or larger, must be less than 100. The known number[2] of Apollos in this size range is currently about $6\times$ larger.

The lesson from these early attempts to debias the observed population is that correcting for observational selection effects is not easy. It is not appropriate to make simple single-parameter (e.g. absolute magnitude) corrections because there is a complicated interplay between the parameters that determine whether an asteroid will be detected by a survey and the underlying orbit element and size–frequency distribution.

Spahr (1998) and Jedicke and Metcalfe (1998) independently and nearly at the same time implemented the first 'modern' attempts to simultaneously compensate for main belt asteroid survey selection effects in the 4-dimensions of semi-major axis, eccentricity, inclination and absolute magnitude. The former work re-calculated the observational biases for the PLS and also applied their method to a new survey optimized for detecting high-inclination objects. The latter work was used to determine the biases in the Spacewatch near-Earth object (NEO) survey (e.g. Larsen et al., 2001) and to fit the observed NEO distribution to a theoretical NEO model (Bottke et al., 2002). They predicted that there were 960 ± 120 NEOs with $H < 18$, about 2-σ below the almost 1200 NEOs now known in that size range. The NEO population is thought to be $\gtrsim 90\%$ complete so it is unlikely that the (Bottke et al., 2002) result will turn out be in error by more than a few sigma. The 40% error in the Bottke et al. (2002) NEO model is more than $10\times$ less than the $\sim 600\%$ error in the Whipple's (1973) prediction from 30 years earlier and it is desirable to reduce the error in future models that extend the size distribution to smaller asteroid sizes.

There are two main problems in calculating survey biases for asteroids. First, asteroid surveys have focussed more on ambitiously discovering new objects at the expense of rigorously quantifying their detection capability as a function of apparent magnitude and rate of motion. These are the two main observables that determine whether an asteroid is discovered and they depend directly on the object's orbit and physical characteristics and are required for an accurate determination of the bias. Second, it is computationally expensive to calculate a survey's asteroid detection efficiency (bias correction). The calculation is even more complicated for comets because of their variable phase functions and the problems associated with detecting 'fuzzy' image features or those with tails and even more complicated morphologies.

In this work we mostly address the computational issue by introducing a method that efficiently determines the orbit element phase space of objects that can appear in a field, thereby eliminating the need to calculate ephemerides for objects that never do. We apply the method to the Catalina Sky Survey for NEOs (Christensen et al., 2012; Larson et al., 1998) because they have measured their detection efficiency on a nightly basis and characterized it as a function of a detection's trail length.

2. Survey bias

In this section we define and derive our calculation of an asteroid survey 'bias' that is a correction factor from the observed number of asteroids to the actual number in a desired sub-population.

Let $\vec{x} \equiv (a, e, i)$ represent an asteroid orbit's semi-major axis a, eccentricity e, and inclination i, while $\vec{y} \equiv (\Omega, \omega, M)$ represents the orbit's angular elements; the longitude of ascending node Ω, the argument of perihelion ω, and mean anomaly M. Let H represent the asteroid's absolute magnitude.[3] Furthermore, let $\vec{z} \equiv (\vec{x}, \vec{y}, H) = (a, e, i, \Omega, \omega, M, H)$ represent the set of six elements and H. Then the detected number of objects in a single field of view (FOV) j in an infinitesimal range $[\vec{z} - d\vec{z}/2, \vec{z} + d\vec{z}/2]$ is

$$n_j(\vec{z}) \, d\vec{z} = \epsilon_j(\vec{z}) \, N(\vec{z}) \, d\vec{z} \tag{1}$$

where $d\vec{z} \equiv (da, de, di, d\Omega, d\omega, dM, dH)$, $N(\vec{z}) \, d\vec{z}$ is the actual number of objects in the same range of $\vec{z}$, $\epsilon_j(\vec{z})$ is the efficiency for detecting objects with $\vec{z}$ in the field, and $N(\vec{z})$ and $n_j(\vec{z})$ are the actual and observed number densities at $\vec{z}$.

The actual distribution of objects $N(\vec{z})$ can only be determined with a good measurement of the efficiency and a large number of detected objects. Since the number of objects in any single FOV is small, and the efficiency of detecting them is explicitly a function of their apparent brightness and rate of motion and only implicitly dependent on the orbit elements and absolute magnitude, the calculation of $N(\vec{z})$ typically requires a large number of fields j and an accurate measurement of the detection efficiency. Thus, the total number of detected objects n' in an infinitesimal range $[\vec{z} - d\vec{z}/2, \vec{z} + d\vec{z}/2]$ detected during a survey with many fields of view is

$$n'(\vec{z}) \, d\vec{z} = \sum_j \epsilon_j(\vec{z}) \, N(\vec{z}) \, d\vec{z} \equiv b(\vec{z}) \, N(\vec{z}) \, d\vec{z}. \tag{2}$$

In this formulation we allow that the same object may be detected multiple times in different fields and we introduce $b(\vec{z})$, a correction factor from the number of detected objects with $\vec{z}$ in all the fields to the actual number of objects with $\vec{z}$ in the population.

At the current time there are about 500,000 known asteroids so that if the orbits were randomly distributed, and there were just ten bins in each dimension of a 6-dimensional orbit element space $(a, e, i, \Omega, \omega, M)$, there would be only about 0 or 1 entry in each bin, i.e. there is not much resolution in each dimension even with $\mathcal{O}(10^6)$ orbits. To increase the resolution in each bin we integrate over a limited range of the dimensions so that the detected number of objects in the range $[\vec{z}_1, \vec{z}_2]$ is

$$n'(\vec{z}_1, \vec{z}_2) \, \Delta\vec{z} = \int_{\vec{z}_1}^{\vec{z}_2} b(\vec{z}) \, N(\vec{z}) \, d\vec{z} \tag{3}$$

where $\Delta\vec{z} \equiv \vec{z}_2 - \vec{z}_1$.

If $\Delta\vec{z}$ is small and b a slowly varying function of $\vec{z}$ we can make the approximation that

$$n'(\vec{z}_1, \vec{z}_2) \, \Delta\vec{z} = B(\vec{z}_1, \vec{z}_2) \, N(\vec{z}_1, \vec{z}_2) \, \Delta\vec{z} \tag{4}$$

where we refer to $B(\vec{z}_1, \vec{z}_2)$ as the survey 'bias', the 'correction factor' from the number of detected objects to the actual number of objects $N(\vec{z}_1, \vec{z}_2)$ in the range $[\vec{z}_1, \vec{z}_2]$. Thus,

$$B(\vec{z}_1, \vec{z}_2) = \frac{\int_{\vec{z}_1}^{\vec{z}_2} b(\vec{z}) \, N(\vec{z}) \, d\vec{z}}{N(\vec{z}_1, \vec{z}_2) \, \Delta\vec{z}} \equiv \sum_j \hat{\epsilon}_j(\vec{z}_1, \vec{z}_2) \tag{5}$$

from which it is clear that the bias is the sum over all the survey fields of the number-weighted average efficiency, $\hat{\epsilon}_j(\vec{z}_1, \vec{z}_2)$, for

---

[2] We ignore the ~ 60 sub-components of the disrupted comet 73P/Schwassmann–Wachmann 3.

[3] We use the IAU standard H-G_{12} system Muinonen et al. (2010) with $G_{12} = 0.5$.

detecting objects with orbits in the range $[\vec{z}_1, \vec{z}_2]$ – but note that the weighting is by the *true* number of objects that is unknown until the observations are corrected for the survey bias in the first place.

2.1. Calculating survey bias

Assuming that the detection efficiency as a function of the orbit elements, $\hat{\epsilon}_j(\vec{z}_1, \vec{z}_2)$, is known the obvious and brute force approach to evaluating Eq. (5) is a Monte Carlo method in which many synthetic objects are generated in $\vec{z}$-space according to the as-yet-unknown $N(\vec{z})$ distribution and determine whether they appear in any of the survey fields and, if so, whether they would be detected. Forgetting for a moment that the underlying distribution is unknown, or assuming that a suitable approximation could be developed, the synthetic objects could be generated randomly or on a grid – the latter method is computationally faster and probably better because it eliminates the time required to generate the random number and ensures that the distribution is uniform even for a small number of generated values. Given that the uncertainty on the derived efficiency is $\Delta\epsilon = \sqrt{\epsilon(1-\epsilon)/N}$ then the maximum uncertainty is in those bins with $\epsilon = 0.5$ and we need to generate 2500 synthetic objects in each $\vec{z}$ bin in order that the efficiency uncertainty <1% in all the bins.[4] Thus, we see that even if only 100 bins are used in each of the 6 orbit element dimensions we would need to generate $\mathcal{O}(10^{16})$ synthetic objects and each one of them must be examined to determine if they can appear in any of the survey fields – and there are 100s of thousands of fields in the case of the Catalina Sky Survey for NEOs discussed below (Christensen et al., 2012; Larson et al., 1998). Thus, in this section, we discuss several assumptions and approximations to reduce the problem to a more manageable level where we can evaluate Eq. (5) numerically. Our assumptions are mostly directed to calculating the bias in NEO surveys but may be helpful for other surveys as well.

2.2. Assumptions about the true number distribution

We make several assumptions about the true NEO distribution that we consider to be either obviously reasonable or will justify *a posteriori*:

1. the H, (a, e, i) and (Ω, ω, M) distributions are separable so that $N(\vec{z}) \equiv N(H)f_1(a, e, i)f_2(\Omega, \omega, M)$ where $N(H)$ incorporates the entire number distribution while f_1 and f_2 are normalized, i.e. $1 = \iiint_{\vec{x}} f_1(\vec{x}) = \iiint_{\vec{y}} f_2(\vec{y})$,
2. the efficiency changes linearly over small ranges, or smoothly and slowly, so that if $\langle\vec{x}_0\rangle$ represents the average value of $\vec{x}$ in a small range of $\vec{x} \equiv (a, e, i)$ near $\vec{x}_0$ and $\langle\vec{H}_0\rangle$ represents the average absolute magnitude in a small range of H near H_0 then the detection efficiency over the entire small range of $\vec{x}$ and H is approximately $\epsilon(\langle\vec{x}_0\rangle, \vec{y}, \langle\vec{H}_0\rangle)$,
3. the (Ω, ω, M) distribution is uniform, i.e. $f_2(\Omega, \omega, M) = (2\pi)^{-3}$, and
4. the true number distributions in $\vec{x} \equiv (a, e, i)$ and H change linearly over small ranges, or smoothly and slowly. i.e. $f_1(\langle\vec{x}\rangle) \sim f_1(\vec{x})$ for $\vec{x} \sim \langle\vec{x}\rangle$ and $N(\langle H\rangle) \sim N(H)$ for $H \sim \langle H\rangle$.

The application of these assumptions to other asteroid and comet populations would need to be considered carefully. Populations that are strongly affected by multiple mean-motion reso-

nances would have angular element distributions that are a function of (a, e, i) and limit the applicability of the first and third assumptions.

Our first assumption allows Eq. (5) to be written as

$$B(\vec{z}_1, \vec{z}_2) = \sum_j \frac{\int_{H_1}^{H_2} N(H) \int_{\vec{x}_1}^{\vec{x}_2} f_1(\vec{x}) \int_{\vec{y}_1}^{\vec{y}_2} f_2(\vec{y})\, \epsilon_j(\vec{z})\, d\vec{z}}{\int_{H_1}^{H_2} N(H) \int_{\vec{x}_1}^{\vec{x}_2} f_1(\vec{x}) \int_{\vec{y}_1}^{\vec{y}_2} f_2(\vec{y})\, d\vec{z}}. \quad (6)$$

Note that the first two integrands in the numerator and denominator do not cancel because ϵ_j may depend on all the components of $\vec{z}$. If the range $[\vec{z}_1, \vec{z}_2]$ is small we can implement the second assumption and then

$$B(\vec{z}_1, \vec{z}_2) \sim \sum_j \frac{\int f_2(\vec{y})\, \epsilon_j(\langle\vec{x}\rangle, \vec{y}, \langle H\rangle)\, d\vec{y}}{\int f_2(\vec{y})\, d\vec{y}} \quad (7)$$

where the first two integrands in the numerator and denominator from Eq. (6) now cancel because $\epsilon_j(\langle\vec{x}\rangle, \vec{y}, \langle H\rangle)$ does not depend on $\vec{x}$, and we have eliminated the limits on the integrands for clarity.

Finally, if the range in each element of $\vec{y} \equiv (\Omega, \omega, M)$ is the full $[0, 2\pi]$ and implementing the third assumption

$$B(\bar{a}, \bar{e}, \bar{i}, \overline{H}) = \frac{1}{(2\pi)^3} \sum_j \iiint_0^{2\pi} \epsilon_j(\bar{a}, \bar{e}, \bar{i}, \Omega, \omega, M, \overline{H})\, d\Omega\, d\omega\, dM \quad (8)$$

where we let $(\bar{a}, \bar{e}, \bar{i})$ represent the average values of (a, e, i) and $\overline{H}$ the average value of H in the $[\vec{x}_1, \vec{x}_2]$ range, i.e. a 'bin' in (a, e, i, H)-space. Implementing a non-uniform distribution in (Ω, ω, M) as suggested by JeongAhn and Malhotra (2014) would make little ifference to the remainder of this derivation. Thus, $B(\bar{a}, \bar{e}, \bar{i}, \overline{H})$ is the bias, or correction factor, for the survey near the average $(\bar{a}, \bar{e}, \bar{i}, \overline{H})$ in a small range of $\vec{x}$ and H for all (Ω, ω, M).

We now eliminate the explicit specification of the average terms and write Eq. (8) as

$$B(a, e, i, H) \sim \frac{1}{(2\pi)^3} \sum_j \iiint_0^{2\pi} \epsilon_j(a, e, i, \Omega, \omega, M, H)\, d\Omega\, d\omega\, dM$$

$$\equiv \sum_j \bar{\epsilon}_j(a, e, i, H) \quad (9)$$

and we see that *with* all the assumptions above that the bias as a function of (a, e, i, H) is the sum of the angular-element-averaged per-field detection efficiencies $\bar{\epsilon}_j(a, e, i, H)$.

2.3. Calculating the detection efficiency

The key to evaluating Eq. (9) is to first determine the per-field efficiencies $\bar{\epsilon}_j(a, e, i, H)$. An object with $\vec{z}$ is either in a field j or not. If the object is in the field the probability of detecting it is a function of the object's apparent magnitude m and rate of motion $\dot{\theta}$ where both m and $\dot{\theta}$ depend on $\vec{z}$ and the time at which the field is imaged t_j. Thus,

$$\epsilon_j(\vec{z}, t_j) = \begin{cases} \epsilon_j(m(\vec{z}, t_j), \dot{\theta}(\vec{z}, t_j)) & \text{if object is in field } j \text{ at time } t = t_j, \\ 0 & \text{otherwise.} \end{cases}$$

$$(10)$$

This efficiency is specific to the detection of objects and does not account for whether they are discovered. Restricting the efficiency in the bias calculation to only discovered objects is not a good idea because (1) it dramatically reduces the statistics (many of the identified NEOs are already known) and, perhaps more importantly (2) accounting for whether an object has already been discovered introduces a complicated time-dependence on the 'efficiency for discovery'. In practice, we will assume that every field has the same

---

[4] We use a 1% value only to illustrate the scale of the problem – the actual required uncertainty will depend on the number of detected objects, with the goal being to ensure that the uncertainty in the derived efficiency is much less than the fractional (Poisson) uncertainty in the number of detected objects.
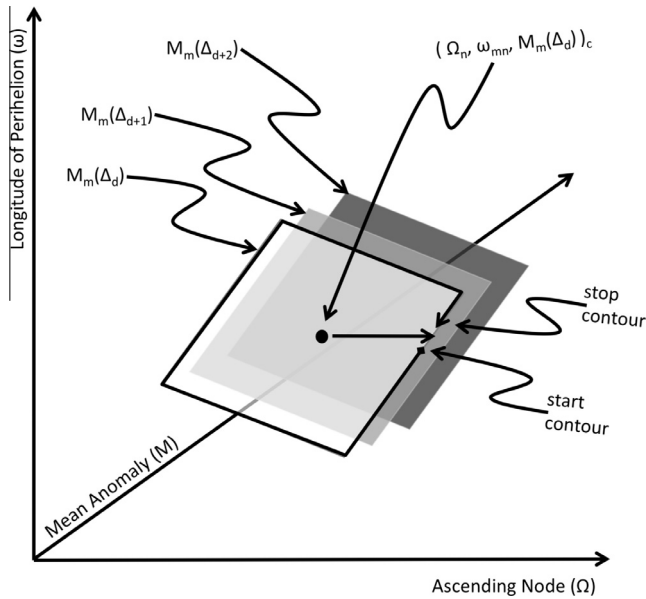
average detection efficiency vs. apparent magnitude and rate of motion (Section 3.2).

Then

$$\bar{\epsilon}_j(a,e,i,H) \equiv \frac{1}{(2\pi)^3} \int_0^{2\pi} dM$$
$$\times \int_0^{2\pi} d\Omega \int_0^{2\pi} d\omega \; \epsilon_j(a,e,i,\Omega,\omega,M,H) \qquad (11)$$

that we translate into the form of a numerical summation

$$\bar{\epsilon}_j(a,e,i,H) = \frac{1}{(2\pi)^3} \sum_{m=1}^{N_m} \Delta M_m \sum_{n=1}^{N_n} \Delta \Omega_n \sum_{l=1}^{N_l} \Delta \omega_l \; \epsilon_j(a,e,i,\Omega_n,\omega_l,M_m,H).$$
$$(12)$$

We allow each step-size in (Ω,ω,M) to have a different value $(\Delta\Omega_n, \Delta\omega_l, \Delta M_m)$ and allow a different number of steps in each angular element (N_l, N_m, N_n) as long as the steps cover the entire range from $[0, 2\pi)$. Performing the summation in Eq. (12) requires many steps over the (Ω,ω,M)-space, most of which produce objects that cannot appear in the field j, so that most of the steps are simply wasted.

Instead, we employ the method outlined in the appendix of Granvik et al. (2012) that, for a specific $(a,e,i,H) \equiv (\vec{x}, H)$, allows us to calculate 4 'central' combinations of $(\Omega,\omega,M)_c$ with $c = 1, 4$ that place an object *on* field j's line-of-sight (LOS, $\hat{\Delta}$, refer to Fig. 1 for vector definitions), i.e. at step d in the direction $\hat{\Delta}$, a distance Δ_d from the observer with $\Delta_q \leqslant \Delta_d \leqslant \Delta_Q$, there are two unique values of the mean anomaly $M_m(\vec{x}, \Delta_d)$ with $m = 1, 2$ where

M_1 is in the range $[0, \pi)$ and M_2 is in the range $[\pi, 2\pi)$. Thus, instead of stepping/summing over mean anomaly in Eq. (12) we, equivalently, make N_Δ steps in Δ in the range $[\Delta_q, \Delta_Q]$:

$$\bar{\epsilon}_j(\vec{x}, H) = \frac{1}{(2\pi)^3} \sum_{d=1}^{N_\Delta} \sum_{m=1}^{2} [M_m(\vec{x}, \Delta_d) - M_m(\vec{x}, \Delta_{d-1})]$$
$$\times \sum_{n=0}^{N_n} \Delta\Omega_n \sum_{l=0}^{N_l} \Delta\omega_l \; \epsilon_j(\vec{x}, \Omega_n, \omega_l, M_m(\vec{x}, \Delta_d), H) \qquad (13)$$

where $M_m(\vec{x}, \Delta_0) \equiv 2M_m(\vec{x}, \Delta_q) - M_m(\vec{x}, \Delta_1)$.

Three steps in $M_m(\vec{x}, \Delta)$ are represented in Fig. 2. At each step in Δ or, equivalently, at a fixed value of the mean anomaly $M_m(\vec{x}, \Delta_d)$, only a limited range of (Ω, ω) is detectable in, i.e. maps into, the FOV. That range is a simply-connected domain in the $M_m(\vec{x}, \Delta_d)$-plane around the central values specified by Granvik et al.'s (2012) algorithm. In this sense the efficiency $\epsilon_j(a,e,i,\omega_l,\Omega_n,M_m(\Delta_d),H)$ is a weighting term on the area with non-zero efficiency in the (Ω, ω)-plane.

Since the FOV is typically small and observable properties of an asteroid change slowly in the narrow *observable* range $[\vec{z}_1, \vec{z}_2]$ within a bin we assume that the detection efficiency does not change much in the non-zero efficiency area around the central (ω_c, Ω_c), i.e. $\epsilon_j(a,e,i,\omega_l,\Omega_n,M_m(\Delta_d),H) \sim \epsilon_j(a,e,i,\omega_c,\Omega_c,M_m(\Delta_d),H)$ for all ω_l and Ω_n. (We will show in Section 4 that this assumption is valid even for the relatively large FOVs in the Catalina Sky Survey.) Letting $\vec{z}_c \equiv (a,e,i,\omega_c,\Omega_c,M_c(\Delta_d),H)$, $A(\vec{z}_c)$ represent the area in the (Ω, ω)-plane where orbits can appear in the FOV, and

Fig. 1. Vector orientations. The perihelion and aphelion distances for an object with semi-major axis a and eccentricity e are represented by q and Q respectively. The heliocentric position of the observer is $\vec{r}_0$ and the topocentric line-of-sight (LOS) is along $\hat{\Delta}$. The heliocentric position of a point a distance Δ from the observer along the LOS is $\vec{r} = \vec{r}_0 + \Delta\hat{\Delta}$, where $\hat{\Delta}$ is the unit vector along the LOS. Thus, the geocentric distance along the LOS (Δ_x) corresponding to a heliocentric distance x (e.g. q or Q) is given by $x\hat{r} = \vec{r}_0 + \vec{\Delta}_x$.

Fig. 2. A cartoon representation of three steps in the numerical integration of the bias in Eq. (13) as discussed in Section 2.3. The central $(\Omega_n, \omega_{mn}, M_m(\Delta_d))_c$ point represents a $\vec{z}$ value that appears on the central line-of-sight (LOS) of a single field-of-view (FOV). At the specified (a, e, i) value there exists a simply-connected domain around the central point in the $M_m(\Delta_d)$ mean anomaly plane in the (Ω, ω, M)-space where objects on those orbits will also appear in the FOV. That region is mapped out using a contour algorithm. Identifying the edge of the contour is illustrated by the right-arrow that locates a $(\Omega, \omega, M_m(\Delta_d))$ point on the edge of the FOV (actually, where the detection efficiency is zero). We then step around the contour to identify the (Ω, ω) boundary of the objects that can appear in the FOV at the current $(a, e, i, M_m(\Delta_d))$.

$\epsilon(\vec{z}_c) \equiv \epsilon(m(\vec{z}_c), \dot\theta(\vec{z}_c))$ represent the detection efficiency in the field for the central orbit, then

$$\bar{\epsilon}_j(\vec{x}, H) = \frac{1}{(2\pi)^3} \sum_{d=1}^{N_\Delta} \sum_{c=1}^{4} [M_c(\vec{x}, \Delta_d) - M_c(\vec{x}, \Delta_{d-1})] A(\vec{z}_c) \, \epsilon(\vec{z}_c) \qquad (14)$$

On the RHS of Eq. (14) the $M_c(\vec{x}, \Delta_d)$ terms are calculated using the method of Granvik et al. (2012), the $\epsilon(\vec{z}_c)$ are determined by the survey properties, and the remaining key is the calculation of the area $A(\vec{z}_c)$.

Fig. 2 illustrates the area $A(\vec{z}_c)$ around the central $(\omega_{mn}, \Omega_n, M_m(\vec{x}, \Delta_d))$ point in the $M_c(\vec{x}, \Delta_d)$ plane. Since the area is a simply connected domain we could map out the area by testing all points on a (Ω, ω) grid around (ω_{mn}, Ω_n) until we identify the relevant area where $\epsilon_j(\vec{z}_{mn}) > 0$. Instead, to save computing time, we use a contour mapping algorithm to identify the edge of the area (Pavlidis, 1982). Starting from $\vec{z}_c$ we increase the ascending node until we identify a point on the contour where the object no longer appears in the field of view (more accurately, where the detection efficiency is zero). We then step around the contour and map out the area $A(\vec{z}_c)$. Thus, we now have all the elements to calculate the survey bias in Eq. (9).

3. Catalina Sky Survey

We will apply the method described above to calculate the survey bias for the two Catalina Sky Survey sites (CSS; e.g. Christensen et al., 2012; Larson et al., 1998; Larson, 2007) that are used in the Granvik et al. (2015) NEO model. The CSS is a NASA-sponsored program dedicated to the search for NEOs. They survey the sky nightly from the Catalina mountains north of Tucson, Arizona (except for the 6–7 days centered on full Moon and a three-month shutdown

Table 1
Catalina Sky Survey site-specific details for the time period of this study (2005 through 2012 inclusive).

Parameter	G96	703
Location	Mt. Lemmon, AZ	Mt. Bigelow, AZ
Longitude	$-110°47.4'$W	$-110°43.9'$W
Latitude	$+32°26.5'$N	$+32°25.0'$N
Telescope	1.5 m reflector	0.69 m Schmidt
Elevation	2790 m	2510 m
CCD	Imager Labs 4096×4096	Imager Labs 4096×4096
Pixel scale	$0.97''$/pixel	$2.5''$/pixel
Field of view	$1.1° \times 1.1°$	$2.85° \times 2.85°$
Typical PSF[a]	$<1.5''$	$<2.0''$
Filter	None	None
Exposure time	Usually 30 s	Usually 30 s

[a] Point spread function.

for the summer monsoon season) using telescopes at two sites that we refer to by their official observatory codes: 703 and G96. Some site details are provided in Table 1 but it is convenient to remember that 703 has a wider FOV but shallower limiting magnitude than G96. Both telescopes were equipped with identical cameras.

Catalina divides the observable sky from each telescope into standard fields that are slightly overlapping and matched to the size of each telescopes' field of view. About 150 of the standard fields are imaged four times each night to identify moving objects. The fields are selected based on the time since last observation and observing circumstances such as airmass, seeing, weather conditions, and Moon position. Site 703 can easily cover the observable sky each month while G96 usually concentrates along the ecliptic and near-Sun regions. Fields near the galactic equator are avoided by both telescopes.

A night of observing is subdivided into 10–15 'sets' of ~10–12 standard fields. Each set is imaged (typically) four times in succession such that observations of individual standard fields in each set are spaced in time by about 10 min. Image data is processed by a moving object detection system where proposed 'tracklets' of detections associated with a single object are validated and reported by a human observer within an hour. Standard image processing for each exposure includes bias correction using data obtained from the CCD overscan regions and flat correction employing 'superflats' assembled from the median average of several hundred images obtained from previous nightss observations. Additional astrometry is obtained for newly discovered objects but CSS maintains a database of field types to distinguish between 'survey' and 'follow-up' fields for subsequent science analysis.

This study used survey fields acquired during calendar years 2005 through 2012 from both telescopes, i.e. we do not include targeted fields in the study, only those fields that were used for 'blind' NEO surveying. The data included the coordinates for the center (boresite) of each field and the mid-exposure times for the first and last images.

3.1. CSS photometry

The CSS has taken special care to ensure that their reported visual magnitudes are as accurate and precise as possible. This is difficult because most of the survey fields do not include suitable standard stars – Landolt standard stars (Landolt, 1983) are only available in a tiny number of CSS fields and are frequently saturated, and the Stetson (2000) standard stars are usually too faint. Furthermore, the unfiltered CSS images introduce a photometric color-dependency.

To combat these problems the CSS extracted a large number of well-distributed Sun-like G0-G8 dwarf stars from the all-sky 2MASS Point Source Catalog (Skrutskie et al., 2006). Since most
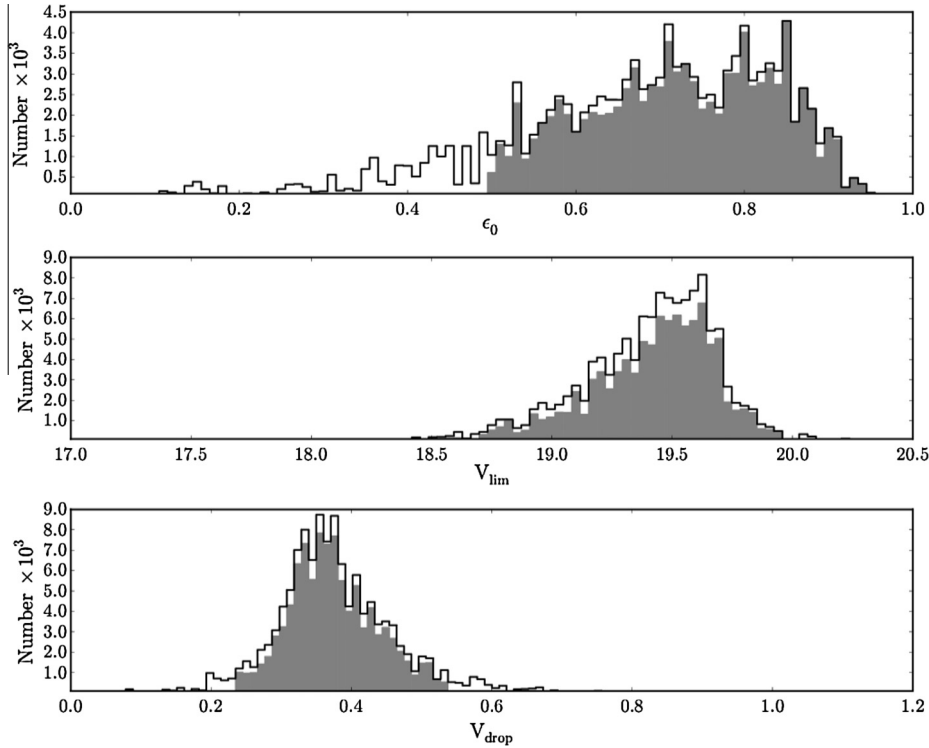
Fig. 3. The CSS 703 site nightly asteroid detection efficiency was fit to a function of the form $\epsilon(V) = \epsilon_0 \left[1 + \exp\left(\frac{V-V_{lim}}{V_{drop}}\right)\right]^{-1}$. The unfilled histogram illustrates the distribution of (top) the maximum efficiency, ϵ_0, (middle) limiting magnitude, V_{lim} and (bottom) drop-off width, V_{drop}, for *all* fields, i.e. nights with many fields have more representation in this figure. The shaded region in each figure shows the set of data that were actually used in the bias calculation.

asteroids are roughly neutral in color their reflected spectra are similar to sunlight so that these stars provide a good color match to the asteroids and they can be used to substantially reduce the uncertainties of their unfiltered photometry. The catalog was further down-selected to only those stars for which the corrected photometric uncertainty in all *JHK* bands was <0.05 mags yielding 10–100 stars per CSS field. The 'homogenized' *V* magnitude of Bessell and Brett (1989) was calculated for each of the comparison stars according to the transformation equations of Skrutskie et al. (2006). Finally, the mean zero-point magnitude for each field was calculated using the method of Henden (2000) that resulted in a field-to-field zero-point *V*-band uncertainty on photometric nights of ~0.06–0.08 mags (valid for most of the asteroids and G-type dwarf stars).

3.2. CSS asteroid detection efficiency

The bias calculation assumes that the asteroid detection efficiency is known at essentially every location in the FOV for all possible rates of motion. This is probably practically impossible. Instead, the CSS calculated an average asteroid detection efficiency for an entire night's set of observations. They used the Minor Planet Center's set of multi-opposition asteroid orbit elements to determine which asteroids should have appeared in each field of view as a function of the objects' *predicted* apparent magnitude: $n_{pred}(V)\Delta V$. They then determined the number of those objects that were actually observed, $n_{obs}(V)\Delta V$, and the nightly efficiency is then given by $\epsilon(V) = n_{obs}(V)/n_{pred}(V)$. The efficiency in each field j on any night was then assumed to be the same as the nightly efficiency.

While this method is practically all that could be hoped to be achieved it does have several obvious problems including but not limited to:

1. the number statistics of known and detected asteroids is dominated by main belt asteroids so that the measured nightly efficiency is really the main belt asteroid detection efficiency,
2. since almost all the detected asteroids are in the main belt there is little dynamic range in measuring the efficiency as a function of the objects' rate of motion,
3. the ephemeris prediction has an intrinsic error that, along with the small offsets in the location of the fields, makes it difficult to know whether all possible detections of an asteroid would actually be in the FOV,
4. the predicted apparent magnitudes will have a systematic offset due to the known systematic offset in the cataloged absolute magnitudes (e.g. Jurić et al., 2002; Oszkiewicz et al., 2012; Pravec et al., 2012; Vereš et al., 2015), and
5. the efficiency can vary dramatically throughout a night due to changing observing conditions and survey strategy.

The nightly efficiency was then fit to a function of the form

$$\epsilon(V) = \epsilon_0 \left[1 + \exp\left(\frac{V - V_{lim}}{V_{width}}\right)\right]^{-1} \tag{15}$$

where ϵ_0 is the detection efficiency for bright unsaturated objects, V_{lim} is the 'limiting' magnitude at which the efficiency drops to 50% of its maximum (i.e. $\epsilon_0/2$), and V_{width} characterizes the 'width' over which the transition occurs from high to low efficiency. Fig. 3 shows that the maximum efficiency varied dramatically at the 703 site from about 10% to >90% though 86% of the nights had $\epsilon_0 > 0.5$. We decided to limit the nights that were actually used to those having parameters within reasonable empirically determined ranges as shown in Table 2. After applying our thresholds we used ~80% of the nights from the 703 site and ~88% of the nights from G96.

Table 2
Limits on nightly CSS efficiency.

Site	ϵ_0			V_{lim}			V_{width}			Pass%[b]
	Min	Avg[a]	Max	Min	Avg[a]	Max	Min	Avg[a]	Max	
703	0.50	0.73	1.0	18.5	19.44	20.0	0.25	0.39	0.55	80.1
G96	0.65	0.88	1.0	20.5	21.15	21.7	0.00	0.41	0.55	87.5

[a] All averages were calculated after all limits were applied and are weighted by the number of fields on nights that meet all the thresholds in this table.
[b] The percentage of all fields imaged on nights that meet these thresholds.
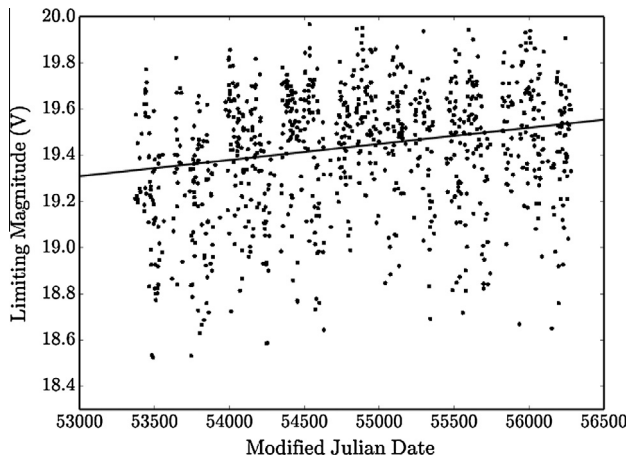
Fig. 4. Nightly limiting V magnitude (V_{lim}) for the CSS 703 site as a function of time for the nights on which the observing efficiency met the requirements provided in Table 2 (shaded values in Fig. 3). The solid straight line is a fit to the data weighted by the number of valid images acquired each night. The slope of the line reflects a real increase in the limiting magnitude with time.

The efficiency is not well-measured at small efficiencies (faint limiting magnitudes) which could introduce dramatic errors into the calculated bias for the faintest objects. We control this effect with a parameter c_{width} (a multiple of the width of the efficiency drop) that sets the efficiency to zero in the bias calculation for $V > V_{max} = V_{limit} + c_{width}V_{width}$. To strike a balance between reducing the number of objects in our sample and our ability to accurately measure the detection efficiency we used $c_{width} = 1$. Finally, we note that the 0.25 mag bin size in the absolute magnitude is on the order of the error induced by the NEO light curve amplitudes.

Fig. 4 shows that the limiting magnitude can change dramatically from night-to-night but also that (1) there are no operations during the summer monsoon season in Arizona, (2) there can be weather-related periods of reduced performance and (3) the 703 site realized a small but statistically robust ~0.2 mag increase in the system limiting magnitude during the 8 years of operations. The improvement is due to typically small but continuous equipment and operational changes and may also be due to long term trends in weather-related sky transparency.

We correct the detection efficiency as a function of the rate of motion ($\dot{\theta}$) using the method of Zavodny et al. (2008) who used CSS data to study objects on heliocentric orbits interior to Earth's orbit. They also faced the problem that the CSS detection efficiency described above, $\epsilon(V)$, is most appropriate to main belt objects. Zavodny et al. (2008) measured the CSS detection efficiency for stars that were artificially trailed at different rates of motion to obtain the trailing correction factor, $\epsilon_{trail}(\dot{\theta}/\dot{\theta}_{MB})$, relative to the efficiency for detecting objects at rates typical of main belt asteroids. We will not consider the detection of objects moving faster than 10 deg/day because most of those objects are identified as trails by the observer rather than the automated detection routines.

The final correction factor compensates for the loss of moving objects because they can move out of (or into) the FOV during the set of exposures used to create tracklets. (A tracklet is a set of observations of the same object obtained in a relatively short period of time, usually about an hour Denneau et al., 2013.) The reported CSS efficiencies already account for the loss of objects at main belt rates of motion ($\dot{\theta}_{MB}$) so we implemented a geometric correction factor, $\epsilon_g(\dot{\theta}/\dot{\theta}_{MB})$. The correction is simply geometric because we know the shape of the field and the rate and direction of motion of the object at each Δ-step in the integration in Eq. (14). One problem with this method is that the measured nightly efficiencies are for main belt objects observed in all fields on the night regardless of their location with respect to opposition, but main belt asteroids' rates of motion depend on their longitude and latitude with respect to the anti-solar point. We simply assumed a fixed rate of $\dot{\theta}_{MB} = 0.23$ deg/day typical of MB asteroids within about 50° of opposition where the CSS surveys typically concentrate their searches (the mean angular distance from opposition of fields obtained in the 703 and G96 surveys is 48° and 52° respectively).

To summarize, in any field j the CSS detection efficiency corresponding to Eq. (10) is $\epsilon_j(V, \dot{\theta}) = \epsilon(V)\, \epsilon_{trail}(\dot{\theta}/\dot{\theta}_{MB})\, \epsilon_g(\dot{\theta}/\dot{\theta}_{MB})$.

3.3. CSS near Earth Objects

The CSS was the most successful NEO survey during most of the time period considered here from 2005 to 2012 inclusive. The two sites combined identified about 6000 (~64%) of the 9444 known NEOs as of 31 December 2012 (see Table 3). They *discovered* 2274 of those NEOs[5] while the others were recovered.[6]

The (a, e, i, H) distributions from the two sites are broadly similar (see Fig. 5) which may be surprising given that the two systems have limiting magnitudes that differ by nearly two magnitudes (see Table 2). One obviously significant difference is the much larger number of low inclination NEOs detected by G96. This is at least in part explained by the difference in survey pattern employed at the two sites – G96 is typically employed closer to the ecliptic due to its smaller field-of-view. The second difference is the upturn in the number of objects with $H \gtrsim 23$ detected with G96 because that site can detect the smaller objects at greater distances due to its superior limiting magnitude. G96's detection efficiency for small objects is further boosted because the apparent rate of motion of the small objects decreases with their geocentric distance as illustrated in Fig. 6. Lower rates of motion mean the objects spend more time in the FOV and suffer less from trailing losses. The figure also shows a clear reduction in the relative number of objects for G96 at fast rates for the same reasons.

Our definition of the bias in Section 2 does not specify that the objects need be unique – it merely sums over all the objects detected in the different fields, so it is possible that the same object may be counted multiple times. Table 3 indicates that only about

---

[5] http://www.minorplanetcenter.net/iau/lists/YearlyBreakdown.html.
[6] We use the total number of identified NEOs rather than discoveries-only as discussed in Section 2.3.

Table 3
CSS NEO tracklets identified on nights that meet the data requirements of Table 2.

Site	Total	Discovered	Discovered %	Unique[a]	Unique[a] %
703	6797	774	11%	2583	38%
G96	5083	1500	30%	3254	64%
Both	11,880	2274	19%	N/A	N/A

[a] Unique to the site.
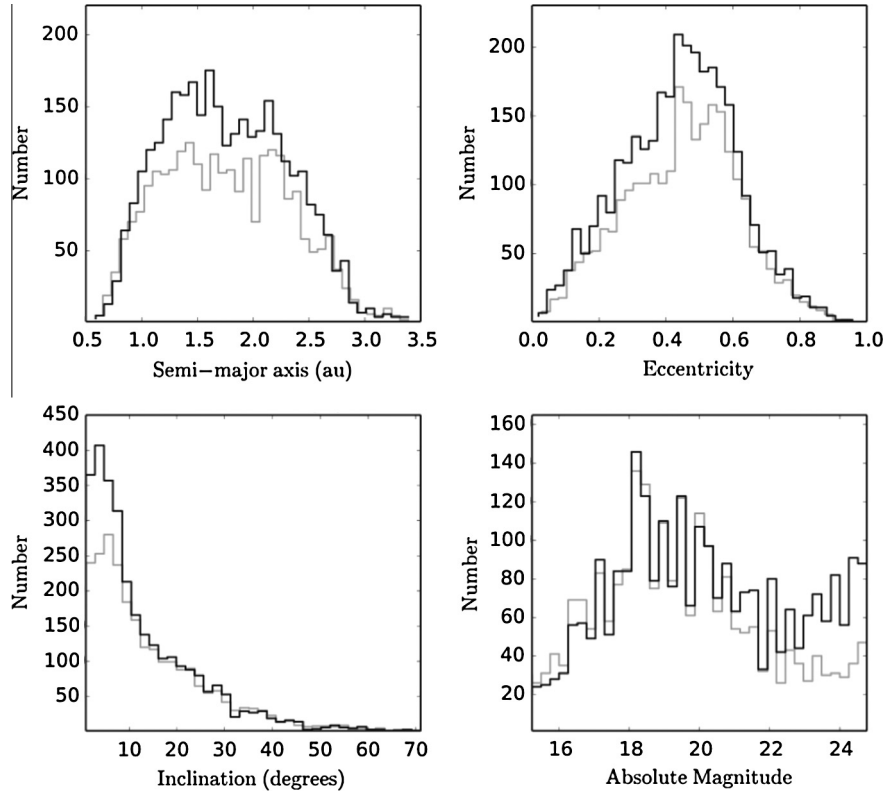
Fig. 5. Clockwise from top-left: the semi-major axis, eccentricity, absolute magnitude and inclination distribution of NEOs detected by 703 (light gray line) and G96 (dark line). The detected NEOs are not unique. (See Table 3 for details.)

25% of detected NEOs at the two sites are unique with G96 yielding less duplication (63%) compared to 703 (75%). This is due to the 703 site having a much wider field of view so that is can cover much larger regions on the sky and is therefore far more likely to re-survey the same region and re-identify the same NEOs.

4. CSS survey bias

In this section we describe how we calculated the bias for both CSS sites for use in creating Granvik et al.'s (2015) NEO model. Their goal was to improve the fidelity and resolution of the Bottke et al. (2002) NEO model for which they required much higher NEO statistics, a better understanding of the NEO sources, and fast bias determination (provided by this work). (We note that Greenstreet and Gladman (2012) made a first step in this direction by re-creating the Bottke et al. (2002) NEO 'residence time' distributions at higher fidelity and resolution.) They fit[7] the observed number of objects $n(a,e,i,H)$ to a NEO model composed of normalized NEO source 'residence time' distributions $R_s(a,e,i)$ for each

source s, the source-dependent NEO size–frequency distribution $N_s(H)$, and the bias:

$$n(a,e,i,H) = B(a,e,i,H) \sum_s N_s(H)\, R_s(a,e,i). \qquad (16)$$

The (a,e,i,H) bias ranges and resolutions were determined by several factors including (1) the actual range of CSS data (see Fig. 5), (2) the resolution at which only one CSS object appears in any bin, (3) the typical uncertainty on the values, (4) the resolution of the dynamical 'residence time' distributions for the NEO source regions and (5) the computing time. We took advantage of the fact that the maximum-likelihood method employed by Granvik et al. (2015) and Bottke et al. (2002) integrates over the entire orbit element space to normalize the likelihood and otherwise uses the bias value *at* the specific (a,e,i,H) value of each detected NEO. This allows us to calculate a 'low' resolution bias for the purpose of normalization. Balancing all these factors we arrived at the ranges and resolutions provided in Table 4 with 13,775 (a,e,i) bins of which roughly 65% are in the NEO range. Even so, and to illustrate the computational problem, since both CSS sites imaged $\mathcal{O}(10^5)$ fields during the time period under consideration, they would require the calculation of $\mathcal{O}(10^9)$ ephemerides if only a single object was generated in each bin.

---

[7] The actual form of the fitting function in Granvik et al. (2015) is more complicated than expressed in Eq. (16) but this form captures the essence of their method.
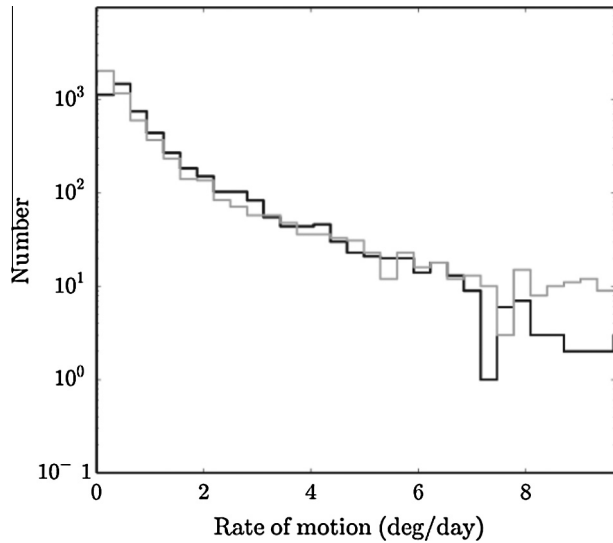
Fig. 6. Rates of motion of NEOs detected by 703 (light gray line) and G96 (dark line). The detected NEOs are not unique. (See Table 3 for details.) The distribution is cut-off at 10 deg/day because objects moving faster than this rate are typically detected by the observer rather than the automated software.

Table 4
Bias calculation ranges and step sizes.

Value	Min.	Max.	#	Size
Semi-major axis (a)	0.6 au	3.5 au	29	0.1 au
Eccentricity (e)	0.0	1.0	25	0.04
Inclination (i)	0°	76°	19	4°
Ascending node (Ω)	0°	360°	N/A	N/A
Long. peri. (ω)	0°	360°	N/A	N/A
Mean anomaly (M)	0°	360°	N/A	N/A
Absolute mag. (H)	15	25	40	0.25

We made several approximations or assumptions in our definition and derivation of the bias in Sections 2 and 2.1 that we now justify for CSS. For instance, in Eq. (2) we allow multiple detections of objects and it could be argued that this will affect the debiasing procedure. Table 3 shows that each NEO was detected on average in 4 separate tracklets. We verified that the number of re-detections is essentially independent of (a, e, i) but the re-detection rate decreases by about a factor of 2 from $H = 15$ to $H = 25$, i.e. as expected, fainter objects are half as likely to be re-detected as brighter objects because they spend less time above the system limiting magnitude. The brightest objects tended to be detected about 5× on average while the faintest objects were only detected about 2.5×. In any event, the double counting is accounted for in our bias correction calculation.

The derivation of Eq. (14) assumed that the detection efficiency at a given (a, e, i, H) and mean anomaly was relatively insensitive to the specific values of ω and Ω that place an object in the FOV. At a particular step in geocentric distance we know that the geocentric distance is constant across the field and only the heliocentric distance and phase angle can change slightly and contribute to modifying the apparent magnitude of an object with fixed H. Thus, we verified that the apparent magnitude of objects at any Δ step changed by $\lesssim 0.05$ mags around the FOV contour. We also verified that the rate of motion around the FOV's contour is roughly constant as illustrated in Fig. 7 – these fields show only a 0.1% change in the rate of motion around the contour despite the wide range of ascending nodes and longitudes of perihelia.

Fig. 7 also illustrates the actual (ω, Ω) contours for real fields that may be compared to our cartoon representation in Fig. 2.

The left/right panels are for objects with inclinations $i = 89.5°/1.0°$ and the top/bottom panels correspond to eccentricities of $e = 0.01/0.2$. Thus, the top-left panel is for a nearly-circular, high-inclination orbit that only allows for a narrow range of allowable (Ω, ω, M). In this case the projection of the FOV into the angular orbit element space is a rhomboid akin to the cartoon concept in Fig. 2. Similarly, the bottom-left panel corresponds to an orbit with slightly higher-than-average eccentricity for main belt objects but the projection of the FOV is still a rhomboid. The situation is dramatically different for objects on low-inclination orbits for which the specified (a, e, i) for the orbit can have a wide range of (Ω, ω, M) in the FOV. In this case the contour mapping out the allowed (Ω, ω) values at a specific mean anomaly assumes a highly elongated 'bananoid' shape.

The range of geocentric distances in Eq. (14) was $[\Delta_q, \Delta_Q]$ with $N_\Delta = 100$ (i.e. 100 steps in geocentric distance) but we used a lower limit on the geocentric distance of $\Delta_{min} = 0.01$ au because the rate of motion changes faster around the (ω, Ω) contour at smaller geocentric distances and because the detection efficiency is only applicable for rates of motion $\dot\theta < 10$ deg/day. NEOs typically have apparent rates of motion of about 10 deg/day when they are about 0.023 au from Earth which is $> \Delta_{min}$ but the actual minimum geocentric distance is not particularly important because our detection is set to zero for $\dot\theta > 10$ deg/day. The maximum geocentric distance in the integration was the value at which the brightest NEO would have an apparent magnitude below the CSS detection limit.

The NEO aphelion limit of 8 au was somewhat arbitrary but incorporates about 99.6% of all known NEOs as of 2013 August 29 including about 99% of all known JFCs. About 7% of the known NEOs are Jupiter Family Comets (JFC) using the definition that JFCs have Tisserand parameters[8] in the range $2 < T_J < 3$. Our aphelion limit of 8 au is equivalent to requiring $T_J > 2.5$ which strikes a balance between incorporating the JFC range into our bias calculation but placing a reasonable limit on the integration in geocentric distance.

The bias calculation software was implemented in Python v2.7.3 with extensive use of Pyslalib v1.0.2 and Numpy v1.7.1. (We understand that our choice of software language results in processing speeds that are considerably slower than what could have been obtained with other common but lower-level languages. It is our intention to re-implement the code in a faster language.) The computations were performed in a data-parallel mode on several clusters accessed through the Finnish Grid Infrastructure environment as well as directly on the alcyone.grid.helsinki.fi (Department of Physics, University of Helsinki) and the vuori.csc.fi (CSC – Scientific Computing Ltd.) clusters. The clusters are built on the 64 bit ×86 architecture using mostly Intel® Xeon® X5650 (2670 MHz) processors (the major exception being vuori.csc.fi which utilizes six-core AMD Opteron™2431 (2400 MHz) processors) and the Linux operating system. The combined amount of individual processor cores in these systems is about 13,300 and we used up to about 1500 of these simultaneously. The biggest challenge concerning the computations was to find a way to ensure that the jobs are finished in the allotted time and that the jobs require a roughly equal amount of processor time to finish. Our final parallelization scheme for the bias calculation was to submit individual bias calculation processes at specific (a, e) combinations, over all H, but with different ranges in inclination. This is because the run time for a (a, e, i) bin was strongly dependent on inclination, small inclinations requiring much more computing time than

---

[8] The Tisserand parameter with respect to Jupiter is given by $T_P = \frac{a_J}{a} + 2\sqrt{\frac{a}{a_J}(1 - e^2)} \cos i$ where a_J is the value of Jupiter's semi-major axis and (a, e, i) are the semi-major axis, eccentricity and inclination of the object.
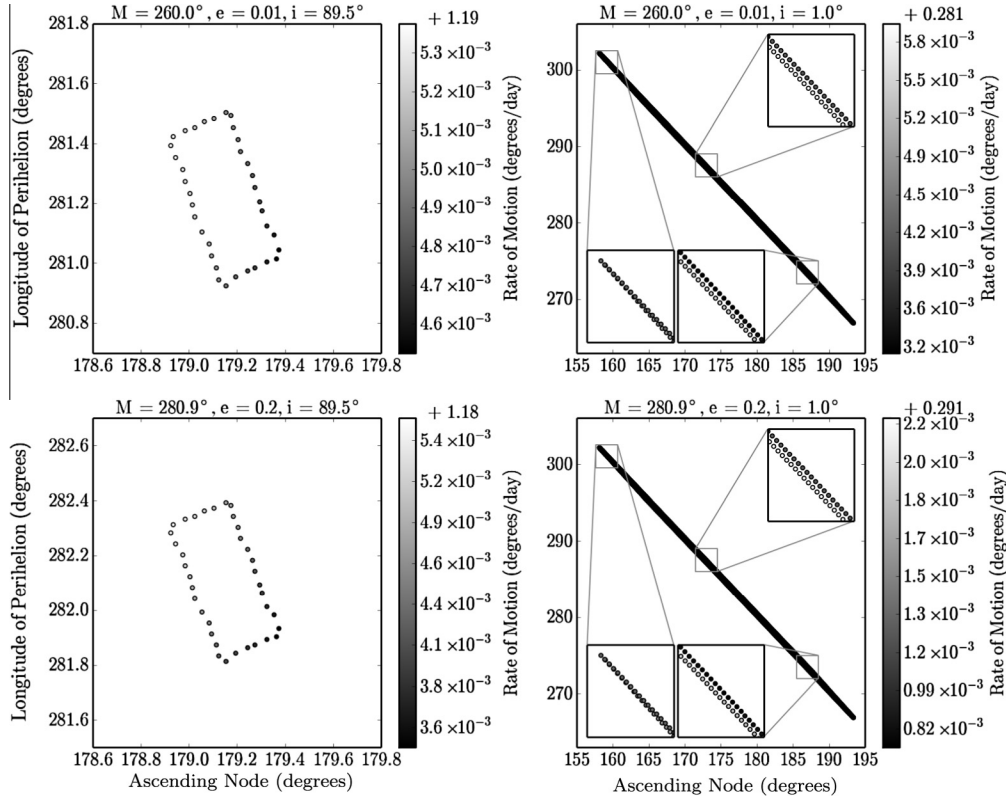
Fig. 7. Realized examples in the bias integration corresponding to the cartoon illustration in Fig. 2 for a $1° \times 1°$ FOV at opposition at the vernal equinox and for an orbit with semi-major axis of $a = 2$ au (see Section 4 for a detailed discussion). The four panels correspond to the step in the bias integration where $r = 2$ au. For the purpose of illustration the points on the contour are much less densely spaced than in our integrations. The gray scale shading of each of the points represent the apparent rate of motion of the object on the orbit on the edge of the FOV.

large inclinations because the FOV's contour was much larger in (ω, Ω)-space as illustrated in Fig. 7. We submitted jobs to the cluster in inclination ranges designed to require roughly the same amount of computing time per job. The G96 grid bias required the submission of 395,850 separate processes and the uncompressed output required about 4 GB of disk space.

In practice, despite the use of a massively parallel super-cluster employed for the bias calculation (described below), we could not explicitly calculate the bias for each field due to computational limitations. Instead, we calculated the bias $B_{lb}(a, e, i, H)$ for each site at 'grid' points in an opposition-centric ecliptic longitude (λ') and latitude (β') system with $\lambda' = l \times 10°$ with $l = 0, 12$ and $\beta' = b \times 10°$ with $b = 0, 7$. Furthermore, we used average values for the detection efficiency in each field rather than field-specific values. This introduced another requirement that all the fields used in the bias calculation, and all the NEOs used in the analysis, be 'average' fields, i.e. generic survey fields rather than targeted followup of specific objects.

The grid bias was only calculated for positive longitudes and latitudes since the bias is symmetric with respect to opposition (Jedicke and Metcalfe, 1998). We then calculated the bias $B_{(\lambda', \beta')}(a, e, i, H)$ for a specific field located at (λ', β') as a weighted combination of the 4 grid biases at the surrounding grid 'corners' denoted as B_g with $g = 1, 4$ ($g = 1$ referring to the lower-left corner and then progressing clockwise through the corners):

$$B_{(\lambda', \beta')}(a, e, i, H) = \sum_g w_g B_g(a, e, i, H) \qquad (17)$$

where the weights w_g are normalized such that $1 = \sum_g w_g$. We examined various weighting methods but the impact on the final

survey bias was always minimal. We settled on a form motivated by a simple 1-d weighting function:

$$f_{\lambda'} = \frac{\lambda' - \lambda'_{min}}{\lambda'_{max} - \lambda'_{min}}$$

$$f_{\beta'} = \frac{\beta' - \beta'_{min}}{\beta'_{max} - \beta'_{min}}$$

$$W_1 = \left[\left[(1 - f_{\lambda'}) + (1 - f_{\beta'}) \right] / 2 \right]^c$$

$$W_2 = \left[\left[(1 - f_{\lambda'}) + f_{\beta'} \right] / 2 \right]^c$$

$$W_3 = \left[\left[f_{\lambda'} + f_{\beta'} \right] / 2 \right]^c$$

$$W_4 = \left[\left[f_{\lambda'} + (1 - f_{\beta'}) \right] / 2 \right]^c$$

$$W = W_1 + W_2 + W_3 + W_4$$

$$w_g = W_g / W$$

where λ'_{min} and λ'_{max} are the bounding opposition-centric ecliptic longitudes, and β'_{min} and β'_{max} are the bounding opposition-centric ecliptic latitudes, of the grid 'box' that includes (λ', β'). This functional form with $c = 8$ reduces the 'contamination' at a grid point by the nearest-neighbor grid point to $\ll 1\%$ in the survey bias (i.e. $\lesssim 3\sigma$).

Several slices through the grid bias are provided in Fig. 8 that illustrate how the bias changes dramatically with (a, e, i, H) and also with the survey location on the sky plane relative to opposition. All the panels represent the normalized bias correction for a single G96 FOV, i.e. normalized bias correction for a $1 \deg^2$ FOV for a specific site. The top two panels are for a FOV at opposition. Note the smoothness of the bias correction over the (a, e)-space indicating that our method introduces little noise. Objects with $e \sim 0$ must have $a > 1$ au in order to be detectable at opposition
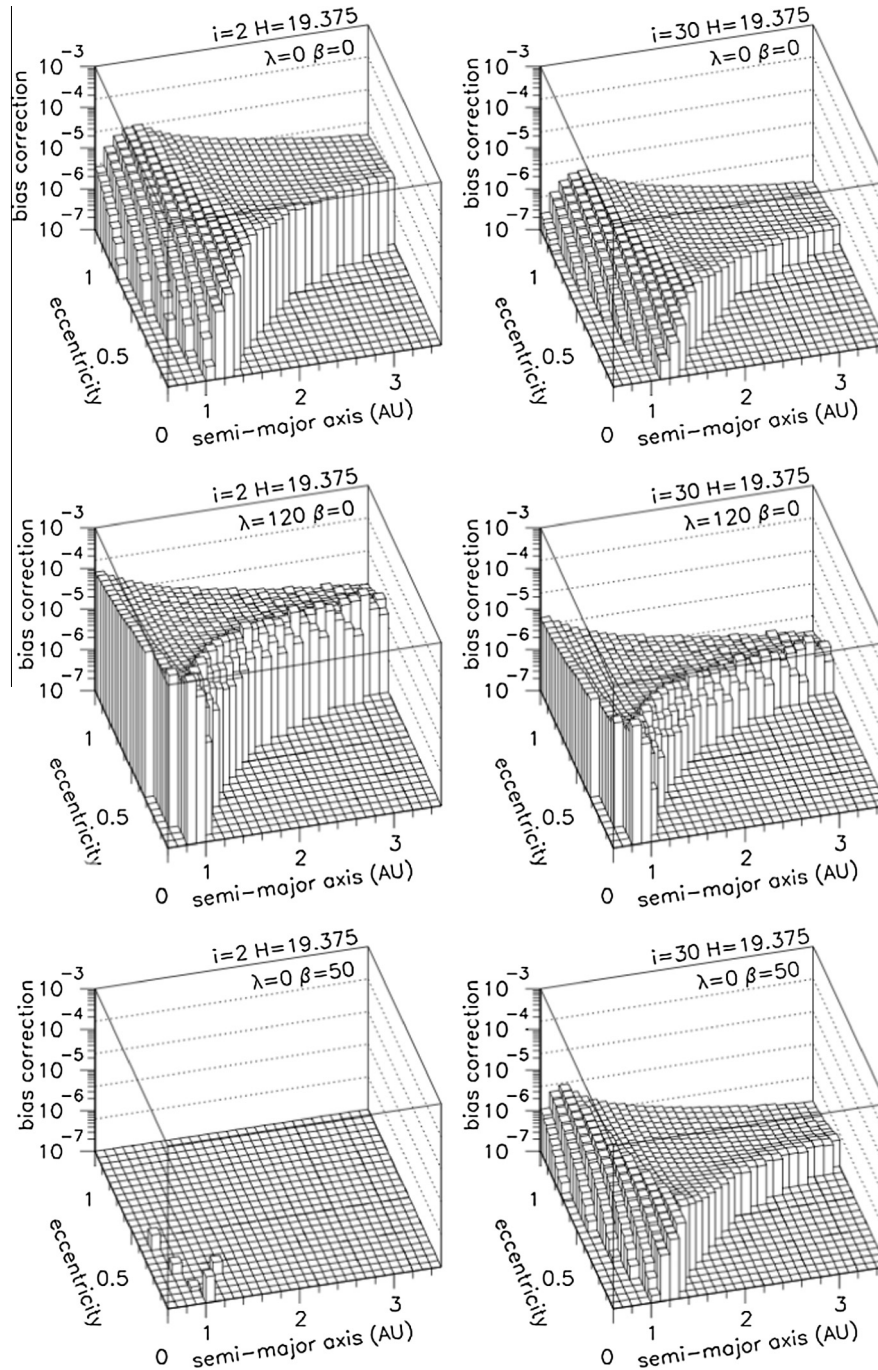
Fig. 8. CSS G96 normalized grid bias corrections (normalized to a 1 deg^2 FOV) as a function of semi-major axis and eccentricity at absolute magnitude $H = 19.375$ (roughly 0.5 km diameter) and inclinations of (left) $i = 2°$ and (right) $i = 30°$ for 3 combinations of longitude (λ') and latitude (β') with respect to opposition: (top row) at opposition where $(\lambda', \beta') = (0°, 0°)$ (middle row) 10° closer to the Sun than quadrature where $(\lambda', \beta') = (100°, 0°)$ (bottom row) 50° north (or south) of opposition where $(\lambda', \beta') = (0°, 50°)$. Note that the maximum bias correction value is 10^{-4} and that we employ a $\log_{10}$ scale. See Section 4 for a detailed discussion.

(see the top-left panel) but at higher inclinations (see the top-right panel) the semi-major axis must be even higher because the high inclination objects with $(a \sim 1$ au, $e \sim 0)$ have high apparent speeds as they pass through the FOV. There is a 'cliff' along the $Q = a(1 - e) = 1.3$ au curve starting at 1.3 au because we have limited our calculation to the NEO region. The top-left panel for $i = 2°$ peaks at about 10^{-5} but the bias correction in the top-right panel peaks at $\sim 0.2 \times 10^{-5}$ for NEOs with $i = 30°$ because high inclination objects spend much less time in fields at opposition (on the ecliptic) than the small inclination NEOs. There is a 'ridge' in both the top panels – at any fixed eccentricity the bias correction

increases with semi-major axis up to the ridge and then decreases slowly (in $\log_{10}$(bias correction)) to the edge of the histogram at $a = 3.5$ au. For instance, at $e = 0.8$ objects can only be detected at opposition if their aphelion > 1 au which requires that $a \gtrsim 0.55$ au. The bias increases with semi-major axis to the ridge because as a increases the objects spend more time in the search volume. The bias decreases with semi-major axis to the right of the ridge because the objects spend less time above the system limiting magnitude.

The middle two panels in Fig. 8 illustrate the bias in a single G96 field when observing on the ecliptic in the 'sweet spots' only 60°

from the Sun (Chesley et al., 2014). This observing orientation allows the telescope to look inside Earth's orbit and detect NEOs on orbits entirely Interior to Earth's Orbit (IEO, e.g. Zavodny et al., 2008). Thus, as illustrated in the middle-left panel of Fig. 8, even low-eccentricity objects with $a < 1$ au can be detected over a wide range of inclinations but the detection of the low-eccentricity objects with $a > 1$ au is essentially zero. These objects might appear in the FOV but would do so at large geocentric distances and large phase angles that make the NEOs faint and therefore difficult to detect. Note that the bias correction peaks at $\sim 10^{-3}$ – nearly two orders of magnitude larger than the largest correction at opposition. Furthermore, the correction decreases as the eccentricity increases at small solar elongations and is a maximum for objects on circular orbits interior to Earth's orbit. There is also a 'ridge' of higher bias correction factors for objects that reach perihelion at about 0.8–0.9 au because these objects spend a longer time and have relatively lower rate of motion when in the FOV. The bias correction has a similar shape for the high-inclination objects (middle-right panel of Fig. 8) but is reduced by about an order of magnitude because they spend less time in the FOV and are moving faster when they do so.

Finally, the bottom two panels in Fig. 8 illustrate how the ecliptic latitude of the survey field (in this case $\beta = 50°$) modifies the observed inclination distribution. Very low inclination NEOs like the $i = 2°$ case in the left panel, on orbits that bring the objects to a heliocentric distance of 1 au can appear in the FOV but when they do so they must be close to Earth meaning that they will have a large apparent rate of motion and be at high phase angle making them much fainter than if they were at opposition. Both effects contribute to the bias being essentially zero for low-inclination objects in high latitude fields. On the other hand, objects on high-inclination orbits (e.g. $i = 30°$ as shown in the right panel) can appear in the same field and will be moving much slower so they stay in the field longer and are more likely to be below the maximum rate cut or suffer significant detection efficiency reduction due to trailing losses.

Since we were unable to calculate the bias for each field, but instead calculated the survey bias from the grid biases as described above, we were unable to use the night-specific efficiencies as described in Section 3.2. Instead, we calculated the grid biases using the average values listed in Table 2 for the parameters of the efficiency function (Eq. (15)). We were concerned that using the average efficiency parameters would create a systematic problem with the bias calculation because the weighted average of a function of several parameters is not equivalent to the value of the function evaluated at the weighted average of each of the parameters. To test the impact of our method we generated 10 'diagnostic' sets of $(\epsilon_0, v_{lim}, V_{width})$ with each parameter generated according to the distributions shown in Fig. 3 within the accepted ranges. We used those parameters to calculate the grid bias at opposition for comparison with the grid bias at opposition calculated with the average parameters. We used the same parameters to calculate the grid bias 100° from opposition on the ecliptic, just 80° from the Sun. It would be best if the average bin-by-bin ratio of the diagnostic biases to the average bias was unity and the average 703 ratios were 1.00 ± 0.09 and 1.04 ± 0.11 at 0° and 100° from opposition on the ecliptic respectively. The equivalent values for the G96 site were 1.08 ± 0.04 and 1.12 ± 0.08 respectively – still within 2σ of unity. Taken at face value, the central non-unitary values in the G96 case implies that there is a difference between the correct field-by-field bias calculation and our average-field grid bias calculation, e.g. the predicted number of NEOs detected by G96 near opposition could be 8% higher using the field-specific efficiencies. The situation is similar for the 1.12 ratio except that very few fields were acquired so far from opposition so the impact on

the overall bias calculation is minimal. Given that this test was of limited statistics, and the method's intrinsic systematic uncertainties, we consider a 2σ agreement to be good and that our method does not introduce significant error into the bias calculation. In any event, we are forced into the approximation due to computing limitations.

Finally, the grid biases were combined as described above to yield the CSS G96 and 703 site survey bias correction as illustrated in eight slices in Figs. 9 and 10 respectively. Several features are visible on the panels in these figures. Large NEOs ($H = 17.875$ or $d \sim 1$ km) on low inclination ($i = 2°$) orbits have a large bias correction with both systems – even the IEOs. As the objects become fainter (proceeding clockwise from the top-left panels) the bias correction decreases quickly such that ~ 100-meter-diameter NEOs ($H = 22.875$) have at best $\sim 10\%$ the correction factor only for the most favorable types of low-eccentricity, low-inclination orbits with semi-major axis just larger than Earth's orbit ($a \sim 1.2$ au). The typical correction factor at $H \sim 23$ is about 1% of the $H \sim 18$ value as might be expected for a ten-fold decrease in size producing a hundred-fold decrease in brightness. At fixed eccentricity the bias correction first increases with semi-major axis but then decreases rapidly beyond a 'ridge' – the location of which mostly depends on the value of the eccentricity and the absolute magnitude. The ridge of largest bias correction moves to smaller semi-major axes for both larger absolute magnitudes and larger eccentricities because objects must be closer to Earth to be efficiently detected.

The two bottom-left panels in Figs. 9 and 10 illustrate the differences between the two CSS site surveys in that even moderate inclination orbits of 10° have ~ 2–$3\times$ smaller correction factors than 2° inclination orbits for the G96 site but the ratio is roughly unity for the 703 site. The difference between the two sites being due to their different survey strategies and capabilities lending emphasis to the necessity of detailed bias corrections when considering a survey's observational results. These ratios may be compared to the relative number of detected NEOs by the two surveys at the same inclinations as illustrated in Fig. 5: ~ 2.5 and ~ 1.0 respectively – but the comparison is not entirely fair because the observed inclination distribution integrates over all a, e and H. Nevertheless, the good agreement between our calculated bias correction ratios at the two different inclinations for the two surveys and the observed number of NEOs is reassuring.

In general, we see that the 703 bias corrections are broadly morphologically similar to the G96 bias corrections except (1) it is usually lower because 703's limiting magnitude is about $V = 19.4$ compared to G96's limit of about $V = 21.1$ and (2) it has higher sensitivity to higher inclination orbits because the 703 survey spends more time surveying at higher ecliptic latitudes because of its wider FOV (average absolute latitude of 6° versus 16°).

The G96 NEO bias correction values combined over all (a, e, i, H) peak near $B = 0.5$ with only $\sim 14\%$ of the values having $B > 0.5$ and less than the maximum correction of $B \sim 7.5$ (see Fig. 11). G96 will tend to detect one out of two NEOs in (a, e, i, H) bins for which the bias correction $B \sim 0.5$ and will tend to make ~ 7.5 detections of each object with an orbit in an (a, e, i, H) bin for where the bias correction $B \sim 7.5$. Large bias correction values are relatively rare because multiple high efficiency detections of the same object are unusual given the survey search pattern – the objects must remain bright enough and unsaturated long enough to be detected often. About 85% of the bias correction values are in the range $0.0001 < B < 0.5$ and only $\sim 1.7\%$ have $B < 0.0001$. The discontinuity in the bias correction distribution near $B = 10^{-4}$ is due to the combination of two factors: (1) we truncate the detection efficiency at a value $\gg 0$ and (2) we are considering a truncated orbit
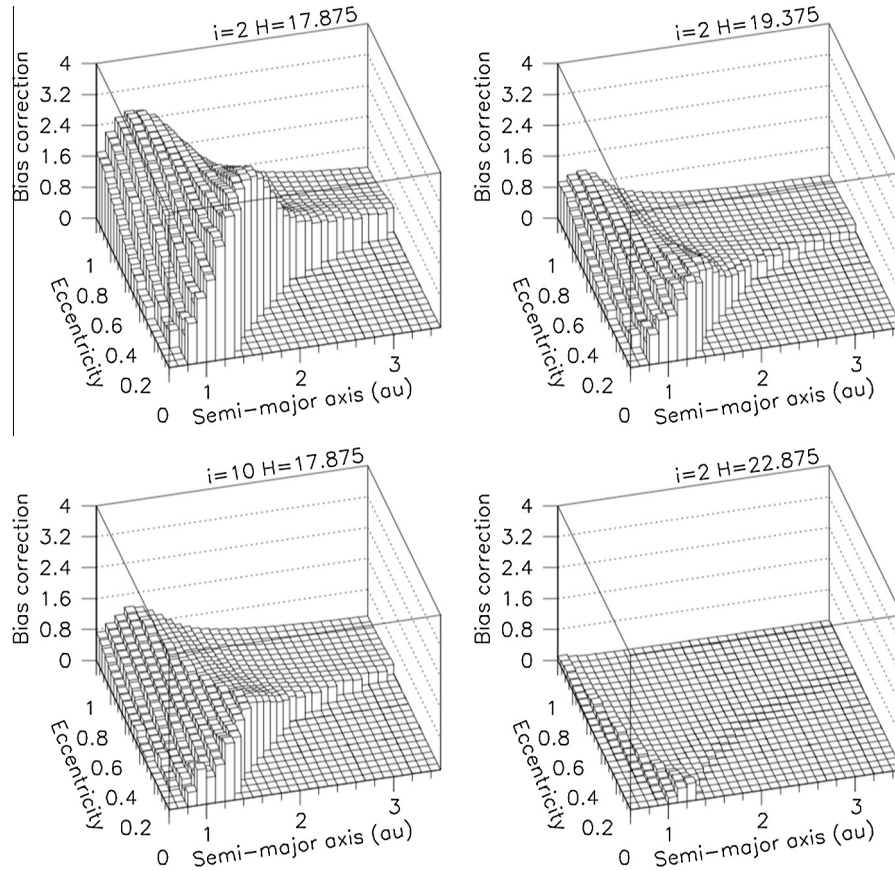
Fig. 9. CSS G96 site survey bias correction as a function of semi-major axis and eccentricity for 4 different (i, H) combinations as shown above each lego plot: reading clockwise – (top left) $i = 2°$ and $H = 17.875$ (top right) $i = 2°$ and $H = 19.375$ (bottom right) $i = 2°$ and $H = 22.875$ (bottom left) $i = 10°$ and $H = 17.875$. See Section 4 for a complete discussion.

element range limited to NEOs with 0.01 au $< q < 1.3$ au, 0.5 au $< Q < 8$ au, $0.6 < a < 3.5$ au. These factors reduce the likelihood of very small bias corrections. The residual corrections with $B < 10^{-4}$ are typically due to small asteroids on unusual orbits that are barely detectable. It should be noted that the minimum $B \sim 10^{-8}$ while the theoretical, smallest possible value for the bias correction is $\sim 10^{-11}$ (as described below in Section 5).

The survey bias correction values for the two CSS sites are available at http://www.ifa.hawaii.edu/cssbias/.

5. Discussion

One of the first tests we made to verify our calculation was to measure the bias for the detection of high-inclination ($i = 89.5°$) main belt objects on circular orbits ($a = 2.0$ au and $e \sim 0$) at opposition in a $1° \times 1°$ FOV. The projection of the FOV into the (Ω, ω)-space under these circumstances is roughly a $0.5° \times 0.5°$ rhomboid as illustrated in Fig. 7, i.e. a $1°$ arc at 1 au as viewed from Earth subtends a $0.5°$ arc at 2 au as viewed from the Sun. The bias should then be about $(0.5°/360°)^2 \sim 1.9 \times 10^{-6}$. Fig. 12 shows that the calculated bias asymptotically approaches that value as the number of steps increases in the geocentric distance (N_Δ). However, the run time increases linearly with N_Δ so we struck a balance between a systematic error in the bias calculation and the run time with $N_\Delta = 100$.

We also performed a direct comparison of our contour method to the 'brute force' Monte Carlo (MC) method by calculating the bias using both methods for; each of the two surveys (G96 and 703); four different fields selected to represent the typical range

of survey locations with $(\lambda', \beta') = (0°, 0°), (+20°, 0°), (+20°, +20°), (0°, +20°)$; and for a range of NEO orbital elements spanning typical Amor, Apollo, and Aten-class orbits with perihelia from <0.1 au to the NEO limit of 1.3 au. In each case we generated synthetic objects until 1000 were *detected* in the field so that the uncertainty on the MC bias was about 3%. The test confirmed that the contour bias method (1) reproduces the MC bias values to within the statistical uncertainty, (2) shows no significant systematic trend with respect to (a, e, i) or q (as addressed by Gronchi and Valsecchi, 2013), and (3) is about $500\times$ faster than the bias method using the same language, base code, and processor.

The smooth variation of the bias as a function of (a, e, i, H) in Figs. 8–10 is a signature of the numerical integration for the bias compared to the brute force Monte Carlo approach. Our method is sensitive to bias correction determinations that are limited by the resolution of the step size in the angular elements (Ω, ω, M) for which the CSS bias calculations used a resolution of $0.01°$ in both the ascending node and argument of perihelion. The resolution in mean anomaly was step size dependent but the average value was about $3.6° = 360°/N_\Delta$. Calculating the bias with the Monte Carlo method at the same resolution would thus require the generation of $\mathcal{O}(10^{11})$ synthetic objects for *every* (a, e, i) bin and every single one of them would require an ephemeris calculation for each of the $\mathcal{O}(10^5)$ fields. On the other hand, our method requires $\mathcal{O}(10^3)$ ephemeris calculations: 5 for both mean anomaly solutions at each of the 100 steps in geocentric distance (see Fig. 2). Since our method maps the (Ω, ω, M)-space that can appear in a FOV for objects with a specific (a, e, i) by identifying the surface of the volume it avoids unnecessary ephemeris calculations for orbits within or outside the volume and can be very efficient when
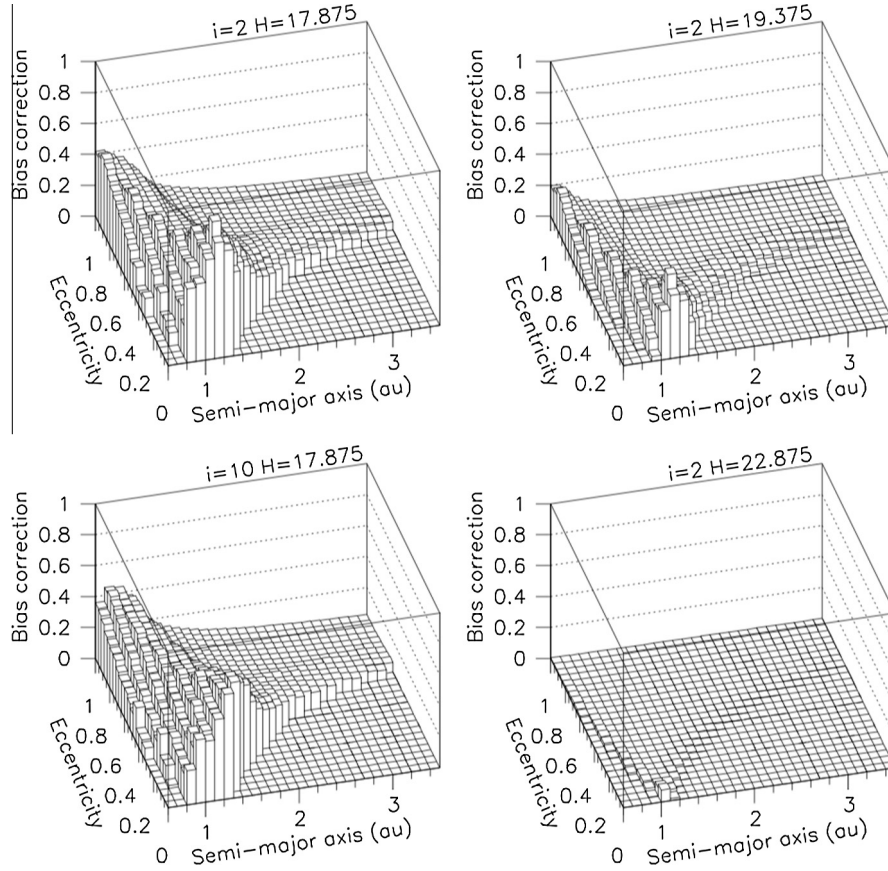
Fig. 10. Same as Fig. 9 except for CSS 703 site and the maximum bias correction value in these figures is 1 instead of 4. The CSS 703 site has a larger FOV, brighter limiting magnitude, and more extensive sky coverage compared to the G96 site. See Section 4 for a complete discussion.
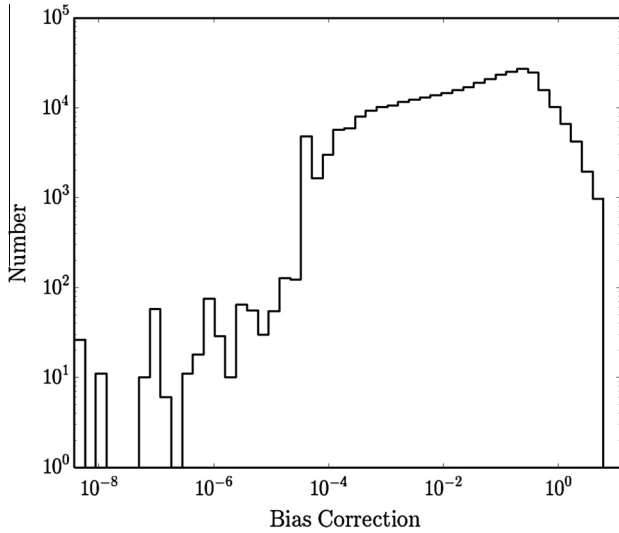

Fig. 11. Distribution of all CSS G96 site survey bias correction values for all (a, e, i, H) bins. The mean value of $\log_{10}$(Bias correction) ~ -0.8 corresponds to a correction of ~ 0.16.

the bias is very small. Furthermore, since we calculate the orbit elements for objects that can appear in the FOV we are always guaranteed to measure the efficiency in every field with non-zero efficiency.

An alternative way of comparing our method with the Monte Carlo method is to calculate the number of generated objects

required to yield the same low 'noise' in the bias. We estimated the 'noise' by fitting the bias as a function of semi-major axes in the range [1.5 au, 3.0 au] at $(e = 0.75, i = 11°, H = 20.375)$ in which the bias values straddle the average value of ~ 0.03 (see Fig. 11). There is no *a priori* functional form for the bias but we found that a 4th order polynomial fits the bias well over those 31 values. The fit would yield $\chi^2 \sim 1$ if the generated number of objects in each bin was $\mathcal{O}(10^5)$. While this is a much more manageable number of objects per (a, e, i) bin it would impose limits on the smallest measurable bias (e.g. where the uncertainty on the bias is 100%) of $b \sim 10^{-5}$ whereas the smallest effective measurable bias correction with our method is $\mathcal{O}(10^{-11})$. Our smallest measured bias correction was almost 3 orders of magnitude larger $(B \sim 10^{-8})$ because the orbit element and observing circumstances required to generate $B \sim 10^{-11}$ are almost impossible given our restrictions on the orbit element phase space and the truncated efficiency curve as described above in Section 4.

Our method imposed several assumptions or approximations to simplify the bias calculation including imposing the survey's average detection efficiency instead of using the per field detection efficiency. That particular problem could be overcome but our study of the systematic issues introduced by the assumption as described in Section 4 suggest that it does not introduce significant errors in the overall survey bias. In contrast, the Monte Carlo method would make it trivial to implement the detection efficiency at any fidelity level.

One of the difficult issues we encountered was dealing with very low inclination orbits and eccentricities (e.g. $i \sim 1°$ and $e \sim 0$). The Keplerian orbital elements are not well behaved in these ranges as the longitude of the ascending node and argument
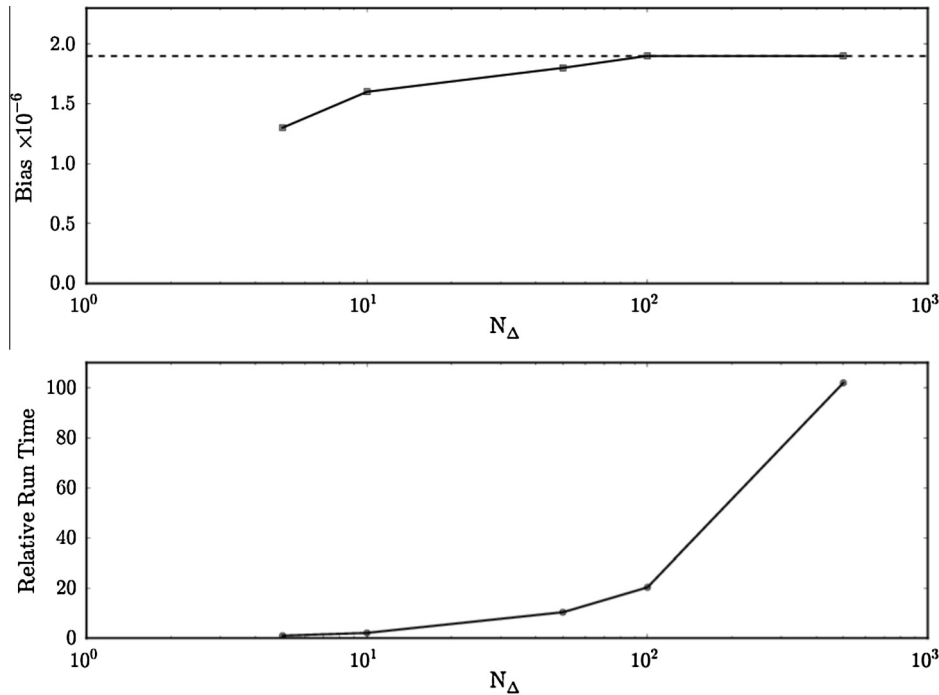
Fig. 12. Bias and run time vs. number of steps in geocentric distance (N_Δ) for the detection of objects with $(a, e, i) = (2\,\mathrm{au}, 0, 89.5°)$. Those types of orbits should have a bias of $\sim 1.9 \times 10^{-6}$ (dashed horizontal line) based on geometrical arguments as described in Section 5.

of perihelion become undefined. This causes difficulty for our contour-mapping algorithm in the (Ω, ω) space at each mean anomaly because the contour becomes very thin, elongated, and often wraps around the $360° \rightarrow 0°$ boundary. On average, the $i = 1°$ bias bins require about $8\times$ more time than the $i = 46°$ bias bins. To avoid these difficulties in the future we will consider using the equinoctial elements (e.g. Broucke and Cefola, 1972) that eliminate the singularities at low a and e.

Asteroid rotational light curves are not taken into account in our method and this will cause problems for asteroids with apparent magnitudes near the survey's magnitude detection limit. In this scenario an asteroid with mean apparent magnitude near the detection limit might be efficiently detected at the peak of its light curve but not detected well at the trough. The effect could be very important for objects with large amplitude variations. The typical main belt asteroid light curve amplitude is $\lesssim 0.3$ mag (e.g. Warner et al., 2009; Masiero et al., 2009) but the light curve amplitude tends to increase with decreasing asteroid size. Asteroids with absolute magnitudes in the range of the NEOs in this study ($H \gtrsim 17.5$) have a mean light curve amplitude of ~ 0.5 mag (e.g. Warner et al., 2009). The mean width of the CSS efficiency drop is about 0.4 mag so that main belt asteroids with light curve amplitudes equal to the main belt mean of 0.3 mag suffer about a 50% change in detection efficiency from min-to-max flux while NEOs with light curve amplitudes of 0.5 mag would have a 100% change in detection efficiency. Since there are more faint than bright asteroids the number of asteroids fainter than the limiting magnitude that can get brighter than the limit is larger than the opposite situation so there is systematic error towards a false increase in the debiased number of objects in the last one or two, 0.25 mag-wide, magnitude bins.

Some unknown NEOs that are brighter than a survey's limiting magnitude may still not be discovered because their rates of motion in longitude and latitude make them indistinguishable from other generic asteroids in the FOV (e.g. Rabinowitz, 1991; Jedicke, 1996). This complicates the process of debiasing a NEO survey because the set of known NEOs that are 'rediscovered' is

complete but the set of unknown NEOs that are discoverable is not. Most surveys employ the Minor Planet Center's 'digest' score[9] as a proxy for the probability that a new set of detections (a 'tracklet') is a NEO and only objects with the highest digest score are targeted for recovery to determine whether they are actually NEOs. The digest score is not actually the probability the object is a NEO – the actual probability drops from >90% at digest $\sim$100 to about 10% at digest $\sim$90. On the other hand, about 75% of NEO tracklets have a digest score higher than the CSS threshold of 50 above which they recover all NEO candidates (calculated with synthetic NEOs detected in a simulated NEO survey described in Denneau et al. (2013)). Since about 81% of all the CSS-detected NEOs are already known (see Table 3) the fraction of NEOs that were unknown and went undiscovered in the CSS data is only about 5%. Since these objects are also mostly like the known NEOs their contribution to skewing the data sample is small.

One method to equalize the treatment of known and newly discovered NEOs is to restrict the bias calculation to only those NEOs of either type that appear in the FOV above a specific digest threshold. On the other hand, for the CSS survey and bias calculation, we know that the largest objects with, e.g. $H \lesssim 18$ are essentially complete so there are no unknown objects in this range. The completeness drops rapidly as the objects become smaller so at first glance it seems much more likely that unknown objects would not be discovered, but the compensating factor is that smaller objects must be closer to Earth and will have higher apparent rates of motion that will make almost all of them easily distinguishable as NEOs. This argument is necessarily an over-simplification of the diverse parameters affecting the apparent rate of motions of objects and the problem of undiscovered NEOs masquerading as MBOs, but the purpose of this work is to describe a practical method of calculating the detection biases in a timely manner. Thus, the end requires the means, and the errors introduced by making these

---

[9] http://www.minorplanetcenter.net/iau/NEO/PossNEO.html.

assumptions are small because only a tiny fraction of orbits yield main belt-like rates of motion for small, nearby objects.

It may eventually be desirable to extend the bias correction calculation to the angular elements (JeongAhn and Malhotra, 2014). Doing so is more problematic from a computing resources standpoint than from the minor modifications required to the algorithm since it will require significantly more computing time and possibly more memory depending on the implementation. Since we write out a file containing the bias correction values, using even just $10°$ wide bins in each of the three angular elements will increase the file size by a factor of almost 50,000 ($36^3=$). Furthermore, the method can easily incorporate other dimensions in the bias correction calculation such as G_{12} or the albedo but, again, the computation time and output file size will increase correspondingly.

Finally, we emphasize that this method may be applied to any asteroid survey from NEOs, as provided here for the Catalina Sky Survey (Christensen et al., 2012; Larson et al., 1998), to distant objects in the solar system like the trans-neptunian or scattered disk objects. The application to comets is problematic only because it is difficult to characterize both the cometary (1) phase function and (2) the detection efficiency. The former issue is difficult because comets have different 'personalities' and do not behave nearly as consistently as asteroids, e.g. comets may experience outbursts in the distant solar system as long-buried volatiles are heated as they approach the Sun. The comet may thus become visible long before an equivalent asteroid or non-active comet at the same distance. The detection efficiency as a function of the comet's brightness is also difficult to characterize – should the nuclear or total magnitude be used? how should the magnitude be measured? how is the detection efficiency modified by the comet's 'fuzziness' or tail? We are confident that these issues can be addressed in a reasonable manner but there is no doubt that they will introduce far more uncertainty than for asteroids and perhaps introduce systematic errors.

6. Summary

We have developed an fast method for compensating for observational selection effects in asteroid surveys and discussed its application to the Catalina Sky Survey for near-Earth objects. Our method allows for either reducing the computation time for the correction factor or decreasing its uncertainty relative to simple Monte Carlo methods or that of Jedicke and Metcalfe (1998). The key to the method is implementing an algorithm developed by Granvik et al. (2012) that calculates the angular elements that place an object with a given semi-major axis, eccentricity and inclination at a specific heliocentric location. The method can easily be applied to calculating the selection effects for any asteroid survey and be adapted to calculating the selection effects as a function of all the orbit elements and to correcting the distribution of observed comets.

References

Baade, W., 1934. On the number of asteroids brighter than photographic magnitude 19.0. Publ. Astron. Soc. Pacific 46, 54–56.

Bessell, M.S., Brett, J.M., 1989. JHKLM photometry: Standard systems, passbands and intrinsic colors. In: Milone, E.F. (Ed.), Infrared Extinction and Standardization, Lecture Notes in Physics, vol. 341. Springer Verlag, Berlin, p. 61.

Bottke, W.F. et al., 2002. Debiased Orbital and Absolute Magnitude Distribution of the Near-Earth Objects. Icarus 156, 399–433. http://dx.doi.org/10.1006/icar.2001.6788.

Broucke, R.A., Cefola, P.J., 1972. On the equinoctial orbit elements. Celest. Mech. 5, 303–310.

Chesley, S.R., Spahr, T.B. 2004. Earth impactors: Orbital characteristics and warning times. In: Belton, M.J.S., Morgan, T.H., Samarasinha, N.H., Yeomans, D.K. (Eds.), Mitigation of Hazardous Comets and Asteroids, p. 22.

Christensen, E. et al., 2012. The Catalina Sky Survey: Current and future work. In: AAS/Division for Planetary Sciences Meeting Abstracts, vol. 44, p. 210.13.

Denneau, L. et al., 2013. The Pan-STARRS moving object processing system. Publ. Astron. Soc. Pacific 125, 357–395.

Granvik, M. et al., 2015. A new model of the near Earth Object population. Icarus.

Granvik, M., Vaubaillon, J., Jedicke, R., 2012. The population of natural Earth satellites. Icarus 218, 262–277.

Grav, T. et al., 2011. The Pan-STARRS synthetic Solar System model: A tool for testing and efficiency determination of the moving object processing system. Publ. Astron. Soc. Pacific 123, 423–447.

Greenstreet, S., Gladman, B., 2012. High-inclination Atens ARE rare. In: AAS/Division for Planetary Sciences Meeting Abstracts, vol. 44, p. 305.05.

Gronchi, G.F., Valsecchi, G.B., 2013. On the possible values of the orbit distance between a near-Earth asteroid and the Earth. Mon. Not. R. Astron. Soc. 429, 2687–2699.

Henden, A.A., 2000. The M67 unfiltered photometry experiment. J. Am. Assoc. Variab. Star Observ. (JAAVSO) 29, 35–43.

Jedicke, R., 1996. Detection of near Earth asteroids based upon their rates of motion. Astron. J. 111, 970–982.

Jedicke, R., Metcalfe, T.S., 1998. The orbital and absolute magnitude distributions of main belt asteroids. Icarus 131, 245–260.

Jedicke, R., Larsen, J., Spahr, T., 2002. Observational selection effects in asteroid surveys. Asteroids III, 71–87.

JeongAhn, Y., Malhotra, R., 2014. On the non-uniform distribution of the angular elements of near-Earth objects. Icarus 229, 236–246. http://dx.doi.org/10.1016/j.icarus.2013.10.030.

Jurić, M. et al., 2002. Comparison of positions and magnitudes of asteroids observed in the Sloan Digital Sky Survey with those predicted for known asteroids. Astron. J. 124, 1776–1787.

Kuiper, G.P. et al., 1958. Survey of asteroids. Astrophys. J. Suppl. 3, 289–428.

Landolt, A.U., 1983. UBVRI photometric standard stars around the celestial equator. Astron. J. 88, 439–460.

Larson, S. 2007. Current NEO surveys. In: Valsecchi, G.B., Vokrouhlický, D., (Eds.), IAU Symposium, vol. 236, pp. 323–328.

Larson, S. et al., 1998. The Catalina Sky Survey for NEOs. In: Bulletin of the American Astronomical Society, Bulletin of the American Astronomical Society, vol. 30, p. 1037.

Larsen, J.A. et al., 2001. The spacewatch wide-area survey for bright centaurs and trans-neptunian objects. Astron. J. 121, 562–579.

Masiero, J. et al., 2009. The thousand asteroid light curve survey. Icarus 204, 145–171.

Muinonen, K. et al., 2010. A three-parameter magnitude phase function for asteroids. Icarus 209, 542–555.

Oszkiewicz, D.A. et al., 2012. Asteroid taxonomic signatures from photometric phase curves. Icarus 219, 283–296.

Pavlidis, T., 1982. Algorithms for Graphics and Image Processing. Computer Science Press.

Pravec, P. et al., 2012. Absolute magnitudes of asteroids and a revision of asteroid Albedo estimates from WISE thermal observations. Icarus 221, 365–387.

Rabinowitz, D.L., 1991. Detection of Earth-approaching asteroids in near real time. Astron. J. 101, 1518–1529.

Skrutskie, M.F. et al., 2006. The Two Micron All Sky Survey (2MASS). Astron. J. 131, 1163–1183.

Spahr, T.B. 1998. Debiasing the Main-Belt Asteroid Population, Ph.D. thesis. University of Florida.

Stetson, P.B., 2000. Homogeneous photometry for star clusters and resolved galaxies. II. Photometric standard stars. Publ. Astron. Soc. Pacific 112, 925–931.

Tedesco, E.F. (Ed.) 1995. EAR-A-5-DDR-UBV-MEAN-VALUES-V1.2. NASA Planetary Data System.

van Houten, C.J. et al., 1970. The Palomar–Leiden survey of faint minor planets. Astron. Astrophys. Suppl. 2, 339–449.

Vereš, P. et al., 2015. Absolute magnitudes and slope parameters for 250,000 asteroids observed by Pan-STARRS PS1 – Preliminary results. Icarus 261, 34–47.

Warner, B.D., Harris, A.W., Pravec, P., 2009. The asteroid lightcurve database. Icarus 202, 134–146.

Whipple, F.L., 1973. Note on the number and origin of Apollo Asteroids. Moon 8, 340–345.

Zavodny, M. et al., 2008. The orbit and size distribution of small Solar System objects orbiting the Sun interior to the Earth's orbit. Icarus 198, 284–293.